Carbon emissions from the edge of the Greenland Ice sheet reveal subglacial processes of methane and carbon dioxide turnover

Jesper R. Christiansen[1*], Thomas Röckmann[2], Maria E. Popa[2], Celia J. Sapart[3†], Christian J. Jørgensen[4]

[1]Department of Geoscience and Natural Resource Management, University of Copenhagen, Denmark.

[2]Institute for Marine and Atmospheric research Utrecht (IMAU), Utrecht University, Netherlands.

[3]Labotorie de Glaciologie, Libre Université de Bruxelles, Belgium.

[4]Arctic Environment, Department of Bioscience, Aarhus University, Denmark

Correspondance to: Jesper R. Christiansen (jrc@ign.ku.dk)

† Current affiliation: CO_2 Value Europe, Belgium.

Key Points:

- Highly elevated CH_4 (up to 250 ppm) and CO_2 (up to 640 ppm) in subglacial air indicate high emissions of both gases from below the ice sheet
- Gaseous CH_4 and CO_2 originate from gases dissolved in the meltwater.
- The isotopic signature and composition of subglacial CH_4 in gas and meltwater show that it originates from microbial acetate fermentation
- Isotopic signatures of subglacial gCO_2 indicate that both methane oxidation and remineralisation are likely subglacial sources of CO_2

Abstract

Emission of methane (CH_4) and carbon dioxide (CO_2) from the subglacial environment under Greenland Ice Sheet (GrIS) was only recently discovered. The understanding of mechanisms and magnitudes of emissions, and the origin of the gases, is extremely sparse. This study reports the magnitude and temporal variations in net emissions at the onset, near maximum and at the end of the melt season in 2018 and 2019 and investigates the possible origin of the subglacial CH_4 and CO_2. *In situ* mole fractions of CH_4 and CO_2 were measured in the subglacial air at a subglacial river outlet where emissions of CH_4 and CO_2 had been identified. Water samples were analysed for dissolved CH_4 and CO_2 concentrations. CH_4 and CO_2 in gas and water samples were analyzed for their isotopic composition of ^{13}C and ^{2}H. Close correlation between gaseous and dissolved CH_4 and CO_2, respectively, show degassing of CH_4 and CO_2 from the subglacial meltwater. The diurnal variability of *in situ* mole fractions of CH_4 and CO_2 in subglacial air was related to meltwater runoff. Maximum *in situ* mole fractions decreased after the peak of the melt season, but estimated net emissions increased because the size of the subglacial river outlet increased. The isotopic signature of CH_4 in the subglacial air, estimated with a Keeling plot, indicated that subglacial CH_4 likely originated from acetoclastic methanogenesis. Isotopic signatures of gaseous CO_2 indicate that both microbial oxidation of CH_4 in the subglacial system and remineralization of carbon in subglacial sediments contribute to subglacial CO_2.

Plain Language Summary

Wetlands and thawing permafrost are considered to be the primary sources of natural methane and carbon dioxide emissions in the Arctic. However, new discoveries show that these gases are also emitted in large quantities from the meltwater coming from under the Greenland Ice sheet. So far, subglacial gas emissions have only been investigated at two sites in Greenland and it is not known how much gas is released, where it comes from and how sensitive the emissions are to future climate change. The aim of our research is to investigate how much is emitted to the atmosphere and what the likely origin of these gases are. Our field measurements show that the levels of methane and carbon dioxide in the glacial outlet cavity are up 100 times higher than the background levels of methane in the atmosphere. Our results show that these gases originate from biological processes under the ice, and that the release rate is controlled by the melting of the glacier. Our study reveals new insight in to this unknown Arctic source of

greenhouse gases which will help us to understand its broader relevance for the atmospheric composition and its feedback to climate change.

1 Introduction

Ice sheets and glaciers separate large parts of the earth's rocky surface and sediment deposits from the atmosphere. Until recently it was perceived that glaciated areas had no significant impact on the glocal carbon cycle and that only little carbon was exchanged across this separating layer. Recent research results have challenged this view by showing that large exports of both methane (CH_4) and carbon dioxide (CO_2) can occur from subglacial environments (Burns et al., 2018; Christiansen & Jørgensen, 2018; Lamarche-Gagnon et al., 2019; Pain et al., 2020). Estimates show that the subglacial CH_4 export in melt water from the Leverett glacier draining the Greenland Ice sheet (GrIS) can rival those of major world rivers (Lamarche-Gagnon et al., 2019). This points to an overlooked, and likely significant, source of CH_4 and CO_2 emissions to the atmosphere, which is a natural constituent of the global carbon cycle that may be affected by global climate change.

Elevated concentrations and biological production of CH_4 in subglacial waters and sediments have been found under glaciers and ice sheets across Canada (Hamilton et al., 2013), Antarctica (Michaud et al., 2017; Stibal et al., 2012), West Greenland (Dieser et al., 2014), Iceland (Burns et al., 2018) and at the center of the GrIS (Christner et al., 2012; Souchez et al., 1995). Once formed under the ice, the CH_4 may either be stored as dissolved gas in the basal meltwater or accumulate as hydrates under high pressure (i.e. solid CH_4 bound in a crystal structure with water molecules) (Wadham et al., 2012) both of which eventually will be exported to the proglacial zone via meltwater rivers and emitted to the atmosphere. Microbial potential to oxidize subglacial biological CH_4 to CO_2 has also been documented in sediment and water samples from below the GrIS and Antarctica (Dieser et al., 2014; Michaud et al., 2017). These findings point to the potential occurrence of widespread subglacial biological processes responsible for production of CH_4 and CO_2 that can be emitted to the atmosphere. Organic carbon reserves in overridden paleosoils (Kohler et al., 2017) or marine sediments (Wadham et al., 2012) below ice sheets worldwide could surpass the amount stored in non-glaciated permafrost areas (Wadham et al., 2019). If this carbon is or becomes available to microbial degradation into CH_4 and CO_2 in the subglacial environment it potentially represents a large, but little known emission magnitude of these gases to the atmosphere.

The very limited empirical evidence from field studies on subglacial CH_4 and CO_2 turnover processes and emissions (Burns et al., 2018; Christiansen & Jørgensen, 2018; Lamarche-Gagnon et al., 2019) is insufficient for understanding of the importance of subglacial carbon conversion for the atmospheric CO_2 and CH_4 composition and whether it can be regarded as potential climate amplifier (Wadham et al., 2008, 2019). In this paper we present new findings from field work carried out in the summers of 2018 and 2019 adding to fill our knowledge gap on subglacial carbon emission rates and turnover processes. We performed *in situ* high frequency measurements of the mole fractions of CH_4 and CO_2 in the subglacial air inside the air-filled ice cavities found at the ice edge, and collected discrete gas and water samples for analyses of the isotopic composition of CH_4 and CO_2. The aims were to 1) measure the magnitude of subglacial carbon fluxes to the atmosphere at the onset, near maximum and late stages of the melt season, 2) to study the diurnal and seasonal temporal dynamics of subglacial CO_2 and CH_4 emissions and their relation with glacial hydrology, and 3) to investigate the potential sources of subglacial CH_4 and CO_2.

2 Materials and Methods

2.1 Site description

The study site is located at an elevation of 450 m above sea level at a lateral subglacial meltwater outlet on the southern flank at the terminus of the Isunnguata Sermia Glacier at the western margin of the GrIS (67°09’16.40’’N 50°04’08.48’’W).

The area in front of the meltwater outlet consists of abraded granodioritic gneiss bedrock with large boulders and patches of gravel, sand and silt deposited by meltwater. The glacier front contained highly irregular cracks and air-filled cavities, which changed over the season as the ice melted and deformed (Figure 1).

The landscape in the Kangerlussuaq area is typical of west Greenland, where numerous, narrow and up to 600 meter deep valleys are oriented in a East - West direction. These valleys extend below the ice sheet, and subglacial valleys can in places reach depths of hundreds of meters below sea level. Deglaciation and re-advance of the GrIS in this region during the Holocene has resulted in buried subglacial carbon rich sediments that were once exposed (Kellerman et al., 2020; Kohler et al., 2017). In the proglacial zone of the study area continuous permafrost extends at places up to 350 meters below the surface (Drake et al., 2017), but the

Isunnguata glacier and GrIS in this area is warm based with an annual ice flow of 150-200 meters and surface meltwater reaching the base of the glacier (Graly et al., 2014).

We sampled melt water and gas at a lateral subglacial outlet to the Isunnguata Sermia glacier draining the GrIS in West Greenland (Figure 1 top panel). The sampling was done during three campaigns covering the periods May 3rd to 6th 2019, June 18th to 28th and August 16th to 24th 2018, during which the cross sectional area of the subglacial outlet changed size and position along the ice edge (Figure 1a-c). These periods are assumed to represent the early, middle and late stages of a typical melt season.

2.2 Measurements of subglacial air velocity, temperature, humidity, atmospheric pressure and water level

At the end of an aluminium pole that extended under the ice for retrievel of unmixed subglacial air we attached instrumentation to measure subglacial air velocity (hot-wire anemometer, model 313-T-DCI-F900-L-O, Onset Computer Cooperation, USA), temperature and humidity (model 313-S-THB-M008, Onset Computer Cooperation, USA). The anemometer was positioned so it measured the wind movement perpendicular to the cross section. Atmospheric pressure was measured outside the cave (model 313-S-BPB-CM50, Onset Computer Cooperation, USA). The data were recorded on a HOBO datalogger (model U30-NRC-VIA-05-S100-000, Onset Computer Cooperation, USA) at 10 second intervals. These measurements were conducted during the June and August campaigns only. We were only able to measure the air velocity for a short period in June as the sensor was damaged by water spray in the ice cave.

During the August 2018 campaign, we also installed an underwater pressure transducer (Onset Computer Corporation, USA) in the outlet stream to estimate the temporal variability of the water level. Air pressure from the meteorological station was used as the atmospheric reference needed to calculate the water level above the pressure transducer. The water level was assumed as a proxy for melt water runoff, but the discharge volume was not estimated.

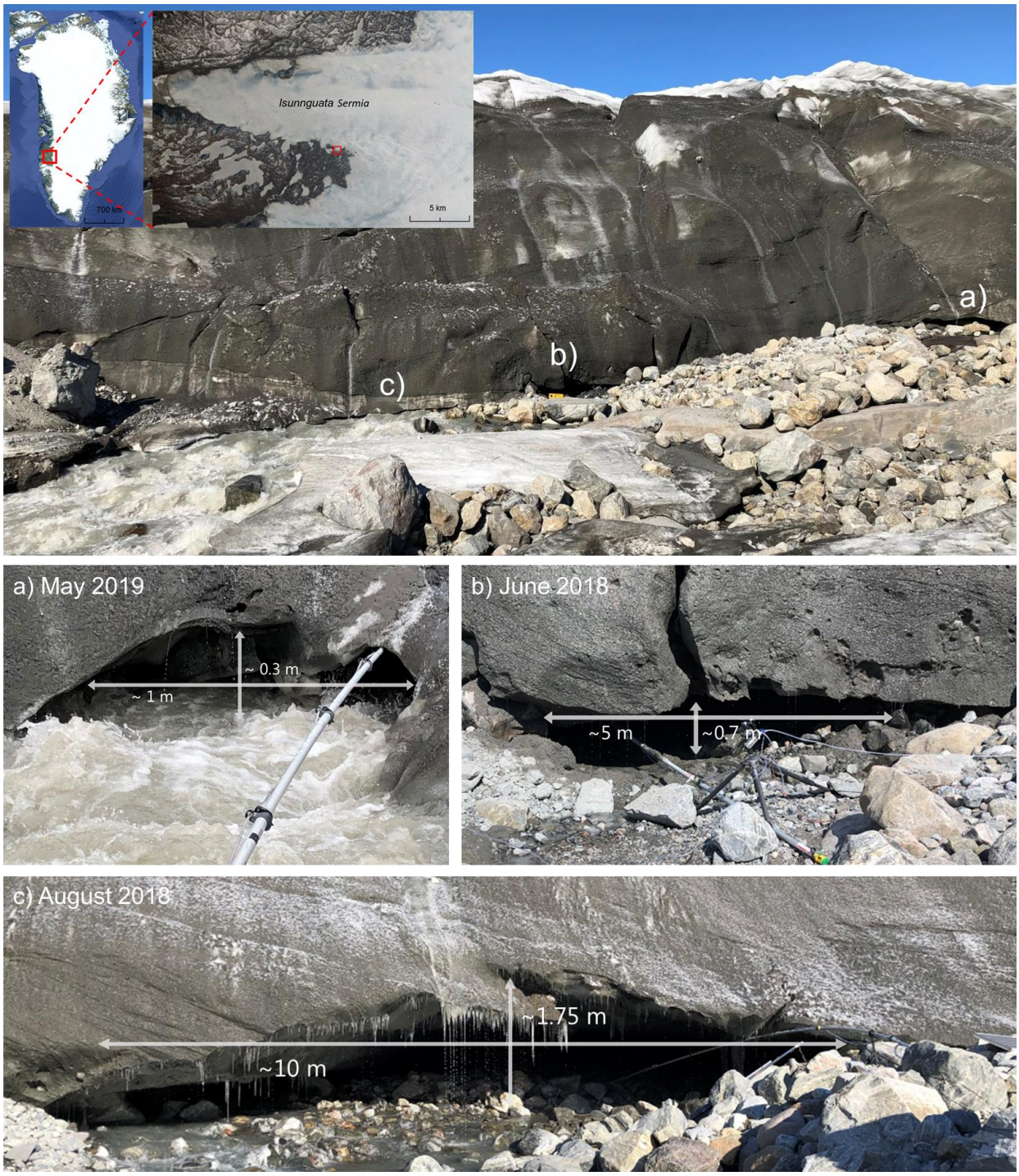

Figure 1 *Top panel: Map of West Greenland and Isunnguata glacier with study site indicated at red squares (top left inset) and an overview of the study site at the ice front in June 2018. Letters (a, b, c) indicate location of measurement of mole fractions of CH_4 and CO_2 in subglacial air and sampling of melt water at three different stages during the melt season. a) May 2019 represents the early stage meltwater discharge where the meltwater openings are small and mostly filled with water. b) June 2018 represents a progressive stage of opening where multiple cracks and caves are air filled after the meltwater has carved out channels in the ice. c) August 2018 represents the mature stage of evolution of the meltwater channel, where the volume of the outlet is at its maximum and most of it is air filled due to decreasing meltwater volumes.*

146 2.3 Measurements of gaseous subglacial CH_4 and CO_2 mole fractions and flux calculation

147 Dry mole fractions of CH_4 and CO_2 in the subglacial air were measured with a portable
148 $CH_4/CO_2/H_2O$ analyzer (Ultraportable Greenhouse Gas Analyzer (UGGA), ABB Los Gatos
149 Research, USA) powered by a 12 V 100 Ah LiFePO4 battery. Due to shifting positions and
150 geometries of the subglacial cave, the gas sampling setup with the UGGA was not identical
151 during all campaigns, but generally followed the same procedure (Figure 1a-c). The cross
152 sectional areas of the outlet during the three campaigns were estimated based on field
153 observations of the dimensions (height and width) of the opening (Figure 1a-c). Gas
154 measurements were performed by attaching a tube to a 9 m aluminium pole and sampling the air
155 inside the subglacial cavities (Figure 1a-c). A water trap fixed to the end of the aluminium pole
156 ensured a liquid free air stream to the gas analyzer.

157 The net CH_4 and CO_2 emission (g CH_4 s^{-1} or g CO_2 s^{-1}) across the entire cross sectional
158 area from the subglacial cave to the atmosphere was calculated as a mass flow of air through the
159 estimated cross section area according to equation 1:

160 $$F_{CO_2/CH_4} = C * \bar{\upsilon} * A * \frac{273.15}{(M_v * T_a)} * M * 10^{-6} \quad \text{(equation 1)}$$

161 Where C is the measured 0.1 Hz dry mole fraction (µmol mol^{-1}) of CO_2 or CH_4, $\bar{v}$ is the wind
162 speed (m s^{-1}) measured every 10 seconds perpendicular to the cross section, A is the cross
163 sectional area at the given measurement period (m^2), M_v is the molar volume (m^3 mol^{-1}), T_a is the
164 air temperature (°K) measured in the cavity, M is the molar mass of CO_2 or CH_4 (g mol^{-1}), the
165 constant 10^{-6} converts the flux from µg to g CO_2/CH_4. The cross sectional area was estimated
166 based on the width and height measured in the field (Figure 1a-c). To estimate and compare the
167 net CH_4 and CO_2 emission between campaigns we assumed that the average wind speed
168 (0.8±0.28 m s^{-1}) measured in June 2018 and air temperature (0.2°C) in the cavity was similar
169 between and constant during the three measurement periods. The average hourly net emission for
170 each measurement period was then calculated as the sum of 0.1 Hz emissions over the
171 measurement period divided by length in hours of the measurement periods. This approach
172 provide at best a rough and uncertain estimate, referred to as "plausible range", and was
173 calculated as the emission for the minimum wind speed at the minimum cross section area and
174 maximum wind speed for the maximum cross section area. The impact of short term influx of

175 CH_4 and CO_2 from the atmosphere to the cave, due to turbulent mixing, was accounted for by
176 averaging the 0.1 Hz effluxes over the measurement period.

177 2.4 Collection of discrete water and gas samples

178 Water and gas samples were taken at three different locations after the subglacial water
179 and air had mixed to different degrees with the ambient environment. For the air samples, the
180 simultaneous variations in mole fraction and isotopic composition were used to determine the
181 isotopic composition of the source (δ^{13}C-CH_4, δ^{2}H-CH_4 and δ^{13}C-CO_2) of the subglacial CH_4 and
182 CO_2 using the Keeling plot approach. This is a widely used method to determine the isotope
183 composition of unknown sources of CO_2 or CH_4 in situations where CH_4 or CO_2 from a source
184 (in our case the subglacial environment) is added to a constant background (atmosphere) (Pataki
185 et al., 2003).

186 Water and gas were sampled twice per day, in the morning and evening, assumed to
187 represent low and high water flow derived from the water level measurements. In 2018, samples
188 were gathered during the periods 22nd – 26th June and 19th – 22nd August.

189 Air samples were collected in 2L gas tight aluminium foil bags (Supel™-Inert Multi-
190 Layer Foil, Sigma-Aldrich, USA) which were filled by a small diaphragm pump. We sampled
191 gas from three locations (Figure 1a-c); inside the ice cave, representing the least mixed
192 subglacial air we could possibly sample (minimal mixing with atmosphere), right outside the ice
193 cave (subglacial air mixed with atmospheric air) and 2 km from the ice edge (background
194 atmosphere, no subglacial air signal).

195 For practical reasons the water was sampled at slightly different positions than the gas.
196 Thus, the first water sample representing the subglacial water was sampled right where the
197 meltwater exists the ice (PW1), the second sample (PW2) 200 meter downstream and the third
198 sample was taken at the same position as the third gas sample, 2 km away from the ice edge
199 (PW3). Unfiltered water was sampled in 120 mL glass bottles with butyl rubber septa and
200 tightened with aluminium screw caps. The bottles were rinsed three times with melt water and
201 filled under water ensuring that no bubbles were included. Immediately after sampling, 12 µL
202 saturated $HgCl_2$ solution was added to the bottles to exclude further biological activity (Magen et
203 al., 2014). Water was sampled in duplicates, one sample for measurement of dissolved CH_4 and
204 another for measurement of CH_4 isotopic composition.

Gas and water samples were stored cold and dark until analysis, except during transport from Greenland to Denmark where samples were transported in the cargo hold of the airplane. Transport resulted in loss of three gas samples, but water samples remained intact. Upon arrival in Denmark the gas bags were immediately sent to Utrecht over land and transferred to glass bottles for longer term storage until isotopic analyses were possible. The total time from sampling to extraction was up to 14 days.

2.5 Dissolved CH_4 concentrations

The dissolved CH_4 was extracted using headspace mixing and the concentration was calculated according to the method outlined in Magen et al. (2014). Shortly, 10 mL of water (V_{HS}) was replaced with CH_4 free N_2 gas and the headspace was afterwards pressurized to 2 atmosphere (P_{HS}), by adding another 10 mL N_2 amounting to 20 mL of gas in the headspace (V_{gas}). The sample was then thoroughly stirred on a shaking table with 150 RPM for three minutes. A 5 mL gas sample was retrieved by syringe from the headspace and transferred to an evacuated 3 mL exetainer with a butyl rubber screw cap (Labco, UK). The pressurization of the exetainer was done to facilitate subsequent gas chromatography analysis. The CH_4 mole fraction in the headspace (CH_4,mf) of extracted gas samples was determined on a gas chromatograph equipped with an FID detector. CH_4 was separated on a HayeSep Q column heated to 60°C, with pure N_2 5.0 as carrier gas. Using a five-point calibration curve the headspace CH_4 mole fraction in ppm was determined. The total dissolved CH_4 was calculated as the sum of the headspace CH_4 and CH_4 still dissolved in the water after shaking (Magen et al. 2014). The ideal gas law was used (laboratory temperature at extraction was 23°C) to convert the headspace concentration to gas amount (mole) (equation 2). The dissolved CH_4 in the remaining 110 mL water was calculated by multiplying the Bunsen coefficient for 0°C (water temperature at sampling) at zero salinity (assumed as we have no data) with the amount of headspace CH_4 to calculate the remaining dissolved CH_4 in water (Yamamoto et al., 1976), accounting for the ratio of water and gas volume (Magen et al., 2014) (equation 3).

$$CH_{4,HS} = CH_{4,mf} * V_{HS} * \frac{P_{HS}}{R*T_{HS}} \ [\mu mol\ L^{-1}] \quad \text{(equation 2)}$$

$$CH_{4,water} = \beta * \frac{CH_{4,conc}*V_{gas}*\frac{V_{water}}{V_{HS}}}{R*T_{water}} \ [\mu mol\ L^{-1}] \quad \text{(equation 3)}$$

Where $CH_{4,conc}$ is the headspace CH_4 mole fraction in ppm, V_{HS} is the headspace volume in L, P_{HS} is the headspace pressure in atm, R is the gas constant (atm L K^{-1} mol^{-1}), T_{HS} is the headspace temperature in °K, β is the Bunsen coefficient, V_{gas} is the total volume of gas in headspace in L, V_{water} is the water volume after replacement in L, T_{water} is the water temperature (similar to T_{HS}).

2.6 Dissolved CO_2 concentrations

Dissolved CO_2 in meltwater was measured *in situ* using an eosGP2 probe (Eosense Inc., Canada) connected to a Campbell CR1000 datalogger (Campbell Scientific Inc., USA) during the June 2018 campaign. The sampling interval was 10 seconds and dissolved CO_2 concentrations given in ppm. A custom calibration for measurements at CO_2 concentrations close to the atmospheric equilibrium had been done prior to the field work by Eosense. Before each deployment, we let the eosGP2 probe equilibrate with the atmospheric background CO_2 concentration for approximately one hour to monitor possible drift and/or sensitivity of the response of the CO_2 signal when switching the probe between the aqueous and gaseous phases. At deployment the eosGP2 probes were fixed in place and the diffusion membrane initially placed 15 cm below the surface of the meltwater at low flow conditions.

2.7 Isotopic analyses of gas and water samples

The isotopic composition of CH_4 ($\delta^{13}C$-CH_4, $\delta^{2}H$-CH_4) was measured using continuous-flow isotope ratio mass spectrometry (CF-IRMS) on a ThermoFinnigan Delta^{plus} XL isotope ratio mass spectrometer. The air samples were injected via a mass flow controller into the sample loop of the extraction system and further processed and analyzed as described in Röckmann et al. (2016). The CH_4 in the water samples was extracted with a headspace mixing method and further analyzed on the same analytical system, as described in Jacques et al. (2020). Further information on the data processing is available in Brass and Röckmann (2010) and Sapart et al. (2011). Specifically, the CH_4 isotopic data were corrected to account for system variability and non-linearity effects and reported in ‰ vs VPDB for $\delta^{13}C$ values and ‰ vs VSMOW for $\delta^{2}H$ values. The measurement reproducibility was calculated from the standard deviation of reference air injections.

The isotopic composition of CO_2 ($\delta^{13}C$ and $\delta^{18}O$) was analyzed with the CF-IRMS

system described in Naus et al. (2018) and Pathirana et al. (2015). This system is primarily meant for CO isotopes, but can also analyze CO_2 isotopes is small samples (~ 2 ml air at normal atmospheric mole fractions). In short, the CO_2 is cryogenically separated from the air, further purified chromatographically, and then injected into the IRMS via an open split inlet. The results are related to the VPDB and VSMOW scales via a reference air cylinder with known isotopic composition. The typical precision, estimated as repeatability of multiple measurements of a constant gas (Target cylinder), is about 3 ppm for the CO_2 mole fractions, and 0.05 ‰ and 0.14 ‰ for $\delta^{13}C$ and $\delta^{18}O$ respectively.

3. Results and discussion

3.1 Subglacial CH_4 and CO_2 mole fractions and concentrations in air and meltwater

Figure 2 shows measured mole fractions of gaseous CH_4 (gCH_4) and CO_2 (gCO_2) (Figure 2a-c) and concentrations of dissolved CH_4 (dCH_4) (Figure 2d-f) for the three campaigns. During all campaigns the gCH_4 and gCO_2 mole fractions measured at the outlet were continuously and significantly elevated compared to the ambient mole fractions of these gases (Figure 2a-c). Also in the water, dCH_4 concentrations are strongly elevated compared to the saturation concentration of CH_4 (0.02 μmol L^{-1}) in contact with ambient air (Figure 2d-f). Collectively, this clearly demonstrates that a source for these gases exists below the ice sheet.

Concentrations of dCH_4 were highest close to the outlet and decreased strongly with distance from the outlet. Degassing is assumed to be the main loss process for dCH_4 from the meltwater between the sampling points PW1 and PW3 (Christiansen & Jørgensen, 2018). Oxidation of dCH_4 to CO_2 can contribute as well, but oxidation rates measured previously are low (Dieser et al., 2014), indicating that it cannot be the main cause for the observed decrease here. The dCH_4 at PW3 occasionally is lower than the atmospheric equilibrium during the June and August 2018 campaigns, but it is not possible to determine if it is attributed to the inherent uncertainty of dCH_4 determination or in-stream oxidation of CH_4 (Figure 2D-E).

In the June and August campaigns both CH_4 and CO_2 showed diurnal variability with some inconsistency between the gases, which indicate that several factors contribute to this observed variability (Figure 2A-C).

In June 2018, the temporal behavior of gCH_4 and gCO_2 were related to variations in melt water and maximum mole fractions of both gases generally occurred at low flow conditions. A possible explanation is that during the period of low water flow less surface water purges the subglacial environment, and the dCH_4 and dCO_2, which presumably, are released at a constant rate from the source under the ice, accumulates in this smaller volume of water, increasing the concentrations. Degassing subsequently enriches the subglacial air with CH_4 and CO_2. Additionally, the increase of melting during the day will dilute the CH_4 and CO_2 bearing subglacial meltwater resulting in lower degassing and hence lower mole fractions in the subglacial air at high water flow. The control of degassing on gCH_4 and gCO_2 mole fractions is supported by simultaneous measurements of gCO_2 and dCO_2 in the June campaign (Figure S2A) and water level for a single diurnal cycle. These measurements showed identical temporal variability of dCO_2 and gCO_2, with maximum dCO_2 and gCO_2 occuring at low flow and higher dCO_2 concentrations relative to gCO_2 (Figure S2) strongly suggesting that the meltwater is the source of gCO_2.

In the August 2018 campaign the diurnal pattern of gCH_4 and partly that of gCO_2 were slightly different than observed in June 2018 and anti-correlated to the flow variations observed in the melt water river in August (Figure S1), with maximum gCH_4 and gCO_2 arriving at the outlet on average 6 hours after minimum flow (Figure S1). At this waning stage of the melt season the internal drainage system has reached its maximum volume, which may not be entirely water filled because of lower melt rates. This could potentially leave air filled subglacial caves where CH_4 and CO_2 can accumulate during low flux and the release to the atmosphere occurs more slowly due to slower transport of the subglacial air compared to the melt water. In the early stage of the melt season, where the drainage system volume is smaller and mostly filled with water, most degassing more likely occurs closer to the outlet. In the May 2019 campaign, where no visible caves had developed at the edge (representing the early melt season) diurnal variability was difficult to discern.

*Table 1 Average, minimum and maximum gaseous subglacial CH_4 and CO_2 mixing ratios in May 2019, June 2018 and August 2018 campaigns. *The enrichment factor (xAtmosphere) relative to the atmospheric background for CH_4 and CO_2 is based on in situ measurements of the atmospheric mole fractions of CH_4 = 2 ppm and CO_2= 400 ppm.*

	CH_4 mole fraction [ppm]				CO_2 mole fraction [ppm]			
	Average	Min	Max	xAtmosphere*	Average	Min	Max	xAtmosphere*
May 2019	70.8	6.67	243	35.4	476	425	580	1.2
June 2018	40.4	8.06	92.1	20.2	521	426	667	1.3
August 2018	18.6	3.68	87.5	9.3	479	397	596	1.2

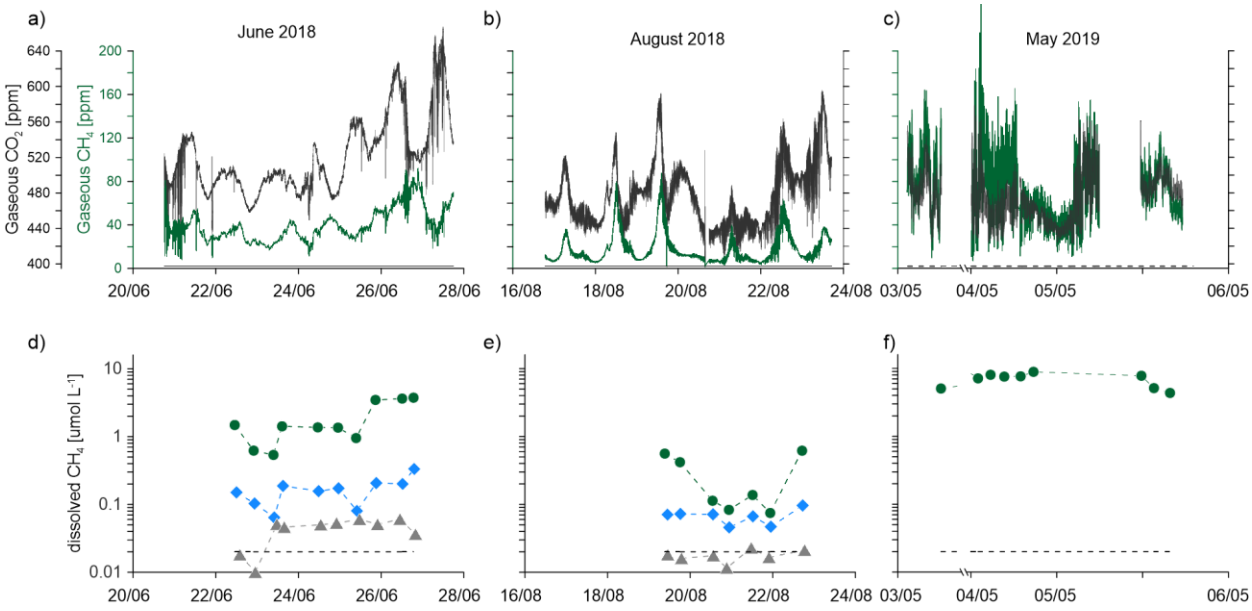

Figure 2 *Upper panels: Time series of subglacial gaseous CH_4 (green) and CO_2 (grey) mole fractions in a) June 2018, b) August 2018 and c) May 2019. Black dashed line indicates the atmospheric mole fractions of CH_4 (2 ppm) and CO_2 (400 ppm) measured on site. Lower panels: Dissolved CH_4 concentrations at three distances (● PW1: 0 m from outlet; ◆ PW2: 200 m from the outlet; ▲ PW3: 2000 meter from the outlet) for d) June 2018, e) August 2018 and f) May 2019. Black dashed line indicates the estimated dissolved concentration of CH_4 at atmospheric equilibrium (0.02 µmol L^{-1}). For interpretation of colours the reader is referred to the online publication.*

Both the level and the temporal variability of gCH_4 mole fractions were different between the seasons, with the highest average and maximum measured in May 2019, followed by June 2018 and the lowest average mole fractions in August 2018 (Table 1, Figure 2a-c). The average enrichment factor (gCH_4/atmospheric CH_4) decreased from May to August from 35 to 9 (Table 1). For gCO_2 there was less difference between the seasons and the average enrichment factor was 1.2 – 1.3 (Table 1). Taking the development of the cross-section area (Christiansen &

Jørgensen, 2018) during field campaigns into account and using the average wind speed ± one standard deviation, it was estimated that the range of hourly CH_4 and CO_2 fluxes increased from May to August (Table 2) despite lower average mole fractions. We note that our total estimate uses several approximations. Notably, we assume constant wind speed of subglacial air and air temperature across the seasonal variation in cross section of the ice cave. It was previously estimated that the subglacial air velocity could reach up to 2 m s^{-1} (Christiansen & Jørgensen, 2018) and in this study we observed fluctuations of the wind speed in this range from 0.1 to 2.5 m s^{-1} (Figure S3) with an average speed of 0.8 m s^{-1} and a standard deviation of 0.28 m s^{-1}. Improving the measurement of the subglacial air velocity is key for more accurate quantification of gaseous flux estimates in the future.

The short-term (minute scale) variability of gCH_4 and gCO_2 was apparently influenced by turbulent mixing with the more dilute atmosphere outside the cave. This was indicated during all campaigns by rapidly fluctuating gCH_4 and gCO_2 mole fractions (Figure 2a-c) and increasing air temperature and decreasing humidity of the subglacial air (Figure S3). However, for most of the time, the relative humidity in the cave remained at 100% and air temperatures were low (below 0.5°C) whereas the outside temperatures were higher (diel variation between 1 - 12°C) indicating an overall low degree of mixing. In particular, the longer-scale diurnal variability is likely not caused by mixing with the outside atmosphere, but by the subglacial supply of trace gases. This is supported by the fact that in August 2018 the subglacial air temperature varied in a pattern that corresponded to the diurnal variation in melt water flow, with highest subglacial air temperatures observed under maximum flow (Figure S3). Whether the higher subglacial air temperature is caused by heat dissipation from frictional heating of the turbulent meltwater or higher influx of relatively warmer surface water is unknown. However, we conclude that the short-term variability of CO_2 and CH_4 mole fractions in the subglacial cave system is a direct product of occational turbulent mixing at the interface between the ice cave and the atmosphere, whereas the diurnal cycle of gCH_4 and gCO_2 and total net emission we observe (Fig. 2A-C) is directly related to the flow of melt water and not the atmospheric conditions outside the cave.

Table 2 Flux range estimates of CH_4 and CO_2 for the non-water filled cross section of the subglacial river outlet for the May 2019, June 2018 and August 2018 campaigns.

	Cross section	Subglacial air	Hourly average	Hourly average

	area	velocity*	CH_4 emission**	CO_2 emission**
Unit	m^2	$m\ s^{-1}$	$g\ CH_4\ h^{-1}$	$g\ CO_2\ h^{-1}$
May 2019	0.30 - 1	0.8	30 – 200	520 – 3620
June 2018	3-4	0.8 ± 0.28	170 – 460	5920 – 16400
August 2018	8 - 10	0.8	200 – 510	14100 – 36610

*Average±standard deviation of measurements for a three day period in June 2018. Used also for May 2019 and August 2018, **fluxes are rounded to the nearest 10.

3.2 Isotopic composition of subglacial CH_4 and CO_2

Figure 3 shows a dual isotope plot of the isotopic signatures ($\delta^{13}C$-CH_4 and $\delta^{2}H$-CH_4) estimated from separated Keeling plots (Figure S4A-D), for gaseous CH_4 and the isotopic composition of the dissolved CH_4. compared to measurements of $\delta^{13}C$ and $\delta^{2}H$ values of discrete gas samples for ambient air. These estimates clearly indicate that dCH_4 and gCH_4 originate from microbial acetate fermentation.

The $\delta^{13}C$ values of dCH_4 at PW1 were depleted compared to the atmosphere and varied little during each campaign and between June and August campaigns, suggesting a similar source over the melt season. The isotopic signature of gCH_4 was slightly enriched in both ^{13}C and ^{2}H and more variable compared to $\delta^{13}C$ values for dCH_4 for most of the June and August (Figure 3, Figure S4).

The isotopic signatures ($\delta^{13}C$ and $\delta^{2}H$) of gCH_4 varied along a line (slopes $\approx$ 5 and 7.4 for June and August 2018 campaigns, respectively) that resembles an oxidation pattern (Figure 3) suggesting *in situ* transformation of the subglacial CH_4. This points to the presence of an active biological system below the ice, but its importance for modifying CH_4 emission to the atmosphere is still unknown. The slope is smaller than what has earlier been attributed to oxidation of dCH_4 (a=8.6-9) (Burns et al., 2018; Etiope & Sherwood Lollar, 2013) and while this indicates that oxidation of subglacial CH_4 takes place, the lower slope for gCH_4 we find suggests additional isotope fractionation processes could impact the isotopic signature of gCH_4. Future research will focus on understanding what drives the deviation between the isotopic signature of gCH_4 and dCH_4 as it has implications for interpretation of the origin of subglacial CH_4.

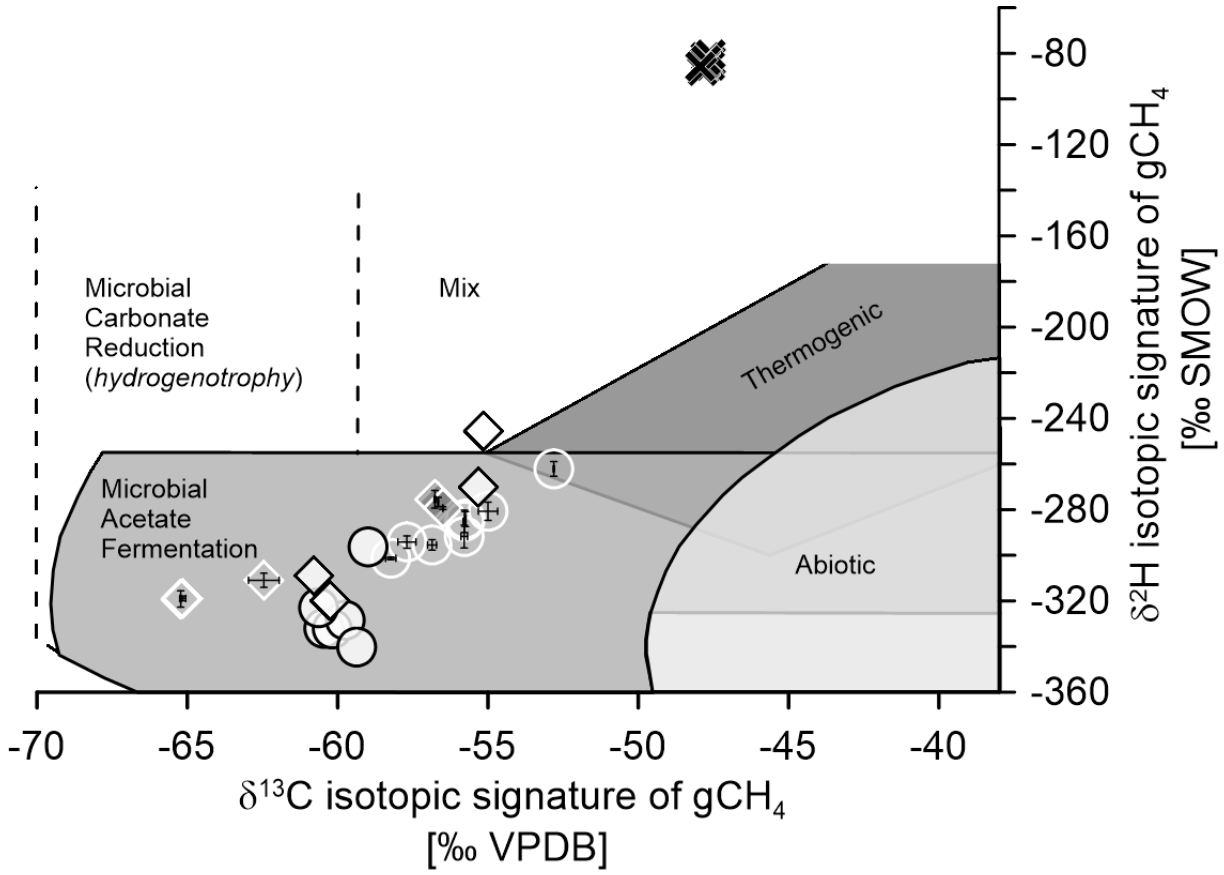

Figure 3 Dual isotope plot of Keeling plot estimates of the isotope source signatures (δ^{13}C-CH_4 and δ^{2}H-CH_4) for gCH_4 (transparent symbols and white marker line) in June 2018 (circles) and August 2018 (diamonds). Standard errors of the estimate of isotopic signature (gCH_4) are shown as error bars. Isotopic composition (δ^{13}C-CH_4 and δ^{2}H-CH_4) of dCH_4 are shown in white symbols with black edge for June 2018 (circles) and August 2018 (diamonds) campaigns. Grey shaded areas modified after Whiticar (1999). For comparison, the δ^{13}C and δ^{2}H values of atmospheric CH_4 are shown with X's.

Further evidence of an active microbial transformation of the subglacial CH_4 and CO_2 emissions is provided by the relation between isotopic δ^{13}C signatures of dissolved and gaseous subglacial CH_4 and of gaseous subglacial CO_2 (Figure 4a & b). The difference (-6 to 22‰) between the δ^{13}C isotopic signatures of gCO_2 and gCH_4, suggests that a substantial proportion of the subglacial gCO_2 is derived from CH_4 oxidation in the subglacial environment (Whiticar, 1999). Using the Keeling plot approach for δ^{13}C of gCO_2 (Figure S5) shows that the samples group in the zone of CH_4 oxidation on the dual isotope plot (Figure 4b). This provides field experimental confirmation for subglacial CH_4 oxidation to CO_2 which in previous studies has only been inferred indirectly (Burns et al., 2018).

We also observed that less δ^{13}C-depleted gCO_2 corresponded to increasing gCO_2 mole fractions (Figure 4a). This cannot be explained by the subglacial CO_2 originating only from CH_4 oxidation, which produces ^{13}C-depleted CO_2 and indicates that one or more additional and isotopically heavier sources of CO_2 contribute to subglacial CO_2. Mixing of subglacial air with isotopically heavier atmospheric CO_2 could in principle enrich the gCO_2 in ^{13}C (as we observed for $\delta^{13}C\text{-}CH_4$), but it cannot increase gCO_2 mole fractions above the ambient level (Figure 2a-c).

Instead, it is possible that the increasing mole fraction and ^{13}C-enrichment of gCO_2 could be due to an increased proportion of gCO_2 (and dCO_2) originating from remineralized subglacial organic carbon (Pain et al. 2020), as the export of dCO_2 from remineralization of organic carbon in subglacial sediments must also be governed by melt flow and subsequent degassing into the subglacial air. Subglacial dissolved organic carbon at this outlet (Andrews et al., 2018), a possible substrate for both methanogenesis and remineralisation, was much more enriched (δ^{13}C-DOC: -29.8 to -24‰) in ^{13}C than subglacial CH_4. Subglacial CO_2 that is originating from this carbon pool should therefore have a higher δ^{13}C isotopic signature than the strongly ^{13}C-depleted CO_2 originating from subglacial CH_4 oxidation.

We observed increasing CO_2/CH_4 ratios in the subglacial air from average values between 5 and 10 in May 2019 to average values >80 in August 2018 (Figure S6). This shows that the export and emission of CO_2 changes during the melt season relative to CH_4 (Figure 2a-c, Table 2), which could be driven by increased CH_4 oxidation and/or remineralisation of organic carbon. As the internal drainage system develops until maximum flow over the melt season, the residence time of the subglacial melt water should increase when the melting decreases later in the year. This longer residence time could enhance subglacial CH_4 oxidation and its contribution to dCO_2, and limit the export and subsequent emission of subglacial CH_4 to the atmosphere. Also, the expanding ablation zone over the melt season connects pockets of subglacial sediment which could not only lead to increased mobilization of CH_4 (Lamarche-Gagnon et al., 2019) (and hence oxidation), but also of remineralization of organic carbon to CO_2 (Kellerman et al., 2020; Kohler et al., 2017). Oxygen availability in the anoxic subglacial environment limits both the oxidation of subglacial CH_4 (Michaud et al., 2017) and remineralization. However, it is plausible that oxygen is supplied to subglacial environments, both from melting of O_2-containing basal ice or import of oxygenated surface melt water. We observed that the subglacial melt water at the outlet was fully oxygenated to nearly 100% of the atmospheric equilibrium during the June 2018

campaign (data not shown) indicating conditions conducive for both processes to occur in the subglacial environment at this site. An additional possible source of subglacial CO_2 could be inorganic carbonate dissolution from the bedrock and the size of this contribution is determined by the endogenous carbonate content of the bedrock and subglacial weathering rates.

Thus, several CO_2 generating processes likely occur simultaneously, and how they contribute to the resulting net emission in the proglacial zone is closely connected to the glacial hydrology and basal distribution of carbon containing sediment and bedrock of the catchment. The interaction between these factors complicates the interpretation of $\delta^{13}C\text{-}CO_2$ values and future research should focus on partitioning the subglacial CO_2 sources (oxidation, remineralization, dilution with atmospheric air, inorganic carbon from carbonate dissolution) using both gCO_2 and dCO_2 together with measurements of subglacial CH_4. This source identification should enable us to narrow in on where in the subglacial system, in transit with the meltwater (Dieser et al., 2014; Lamarche-Gagnon et al., 2019) or at the ice-sediment interface at the subglacial source (Burns et al., 2018; Michaud et al., 2017) the production and release of CO_2 happens.

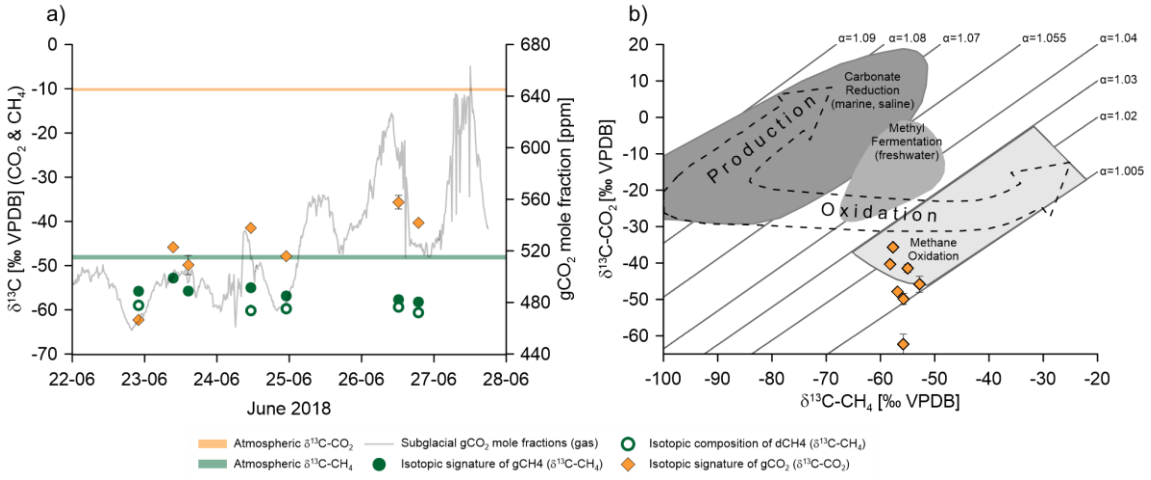

Figure 4 *a) Temporal variation of isotopic ($\delta^{13}C$) source signatures for gaseous CO_2 (◆) and CH_4 (●) and the isotopic composition of dissolved subglacial CH_4 (○). Subglacial gaseous CO_2 mole fractions (ppm) are superimposed as grey line. Vertical error bars for gCO_2 and gCH_4 indicate the standard error of the Keeling plot intercept; in most cases error bars were smaller than the symbols. indicate the $\delta^{13}C$ values of atmospheric CO_2 (orange) and CH_4 (green), respectively and b) Dual isotope plots showing the resulting Keeling plot isotope signature of gCO_2 ($\delta^{13}C\text{-}CO_2$) plotted against the isotopic signature of gCH_4 (orange diamonds). Standard errors of the Keeling plot intercept are shown as vertical and horizontal error bars. In most cases error bars were smaller than the symbols.*

4 Conclusions

In this study we present direct continuous measurements of gaseous evasion of CH_4 and CO_2 from below the Greenland Ice sheet at three different stages of a melt season. These unique seasonal measurements are supported by isotopic studies of both subglacial CH_4 and CO_2 in discrete gas and water samples and show high emissions of CH_4 and CO_2 from the subglacial environment to the atmosphere. Results show that degassing of dissolved gases happens both under the ice in the subglacial cave system and in the proglacial river system confined to a relatively narrow zone from the outlet.

Gaseous CH_4 and CO_2 emissions are closely linked to the glacial hydrology and emissions from the outlet increase over the melt season related to the discharge and development of the subglacial drainage system, allowing more degassing in the subglacial system later in the season. The large emissions of CH_4 and CO_2 point to a significant contribution to the atmosphere. Considering that the phenomenon should also occur at other glaciers along the margin of GrIS and in Iceland, warrants intensified research.

The isotopic signatures show that subglacial CH_4 originates from biological production of CH_4 by acetoclastic methanogenesis, likely from buried organic carbon, which is the source throughout the melt season. Isotopic analysis also shows that the emitted subglacial CO_2 is linked to oxidation of thissubglacial CH_4. However, the isotopic composition of subglacial CO_2 point to other possible sources of subglacial CO_2 apart from CH_4 oxidation and we suggest that remineralisation of organic carbon also contributes to the emission of CO_2 at the outlet. The proportion of CO_2 emission relative to CH_4 increases over the melt season possibly reflects increased oxidation of CH_4 and remineralisation of organic carbon. This is likely fueled by a combination of increased oxygen input from surface water and longer residence time of melt water in the subglacial drainage system. However, it is still unknown where in the subglacial system (sediment, melt water or both) the CH_4 oxidation takes place. The interpretation of the isotope signals suggests that the emitted CH_4 and CO_2 undergo biogeochemical transformation below the ice and that mixing or dilution with other sources during transport under the ice can occur.

Our study shows that large amounts of biogenic CH_4 and CO_2 are emitted from the GrIS via glacial meltwater. However, considerable uncertainty still exists, related to the quantification of the exact mass flux of CH_4 and CO_2 due to an unknown partitioning between aqueous and

gaseous fluxes, as well as uncertainty of the measurement of physical parameters (e.g. wind speed and direction) controlling the net emission. There is a need to advance the fundamental knowledge of the emission of subglacial CO_2 and CH_4 and the biogeochemical processes governing the production and turnover of subglacial carbon to understand this unknown carbon-cryosphere feedback from glaciers and ice sheets worldwide and determine its importance for the atmospheric composition of CH_4 and CO_2.

Data Availability Statement

The data used in this study has been published and can be accessed online through University of Copenhagens Electronic Research Data Archive (ERDA) (at https://doi.org/10.17894/ucph.597b96ab-eef5-4be4-b4dd-b21998e2ed3b)

Acknowledgments

This study was kindly funded by Hartmann Fonden (grant no. A32524). The authors declare no financial conflicts of interests.

References

Andrews, M. G., Jacobson, A. D., Osburn, M. R., & Flynn, T. M. (2018). Dissolved Carbon Dynamics in Meltwaters From the Russell Glacier, Greenland Ice Sheet. *Journal of Geophysical Research: Biogeosciences*, *123*(9), 2922–2940. https://doi.org/10.1029/2018JG004458

Brass, M., & Röeckmann, T. (2010). Continuous-flow isotope ratio mass spectrometry method for carbon and hydrogen isotope measurements on atmospheric methane. *Atmospheric Measurement Techniques*. https://doi.org/10.5194/amt-3-1707-2010

Burns, R., Wynn, P. M., Barker, P., McNamara, N., Oakley, S., Ostle, N., et al. (2018). Direct isotopic evidence of biogenic methane production and efflux from beneath a temperate glacier. *Scientific Reports*, *8*(1), 17118. https://doi.org/10.1038/s41598-018-35253-2

Christiansen, J. R., & Jørgensen, C. J. (2018). First observation of direct methane emission to the atmosphere from the subglacial domain of the Greenland Ice Sheet. *Scientific Reports*, *8*(1), 16623. https://doi.org/10.1038/s41598-018-35054-7

Christner, B. C., Montross, G. G., & Priscu, J. C. (2012). Dissolved gases in frozen basal water from the NGRIP borehole: Implications for biogeochemical processes beneath the Greenland Ice Sheet. *Polar Biology*, *35*(11), 1735–1741. https://doi.org/10.1007/s00300-012-1198-z

Dieser, M., Broemsen, E. L. J. E., Cameron, K. a, King, G. M., Achberger, A., Choquette, K., et al. (2014). Molecular and biogeochemical evidence for methane cycling beneath the western margin of the Greenland Ice Sheet. *The ISME Journal*, *8*(11), 2305–16.

https://doi.org/10.1038/ismej.2014.59

Drake, H., Suksi, J., Tullborg, E. L., & Lahaye, Y. (2017). Quaternary redox transitions in deep crystalline rock fractures at the western margin of the Greenland ice sheet. *Applied Geochemistry*, *76*, 196–209. https://doi.org/10.1016/j.apgeochem.2016.12.001

Etiope, G., & Sherwood Lollar, B. (2013). Abiotic methane on earth. *Reviews of Geophysics*. https://doi.org/10.1002/rog.20011

Graly, J. A., Humphrey, N. F., Landowski, C. M., & Harper, J. T. (2014). Chemical weathering under the Greenland Ice Sheet. *Geology*, *42*(6), 551–554. https://doi.org/10.1130/G35370.1

Hamilton, T. L., Peters, J. W., Skidmore, M. L., & Boyd, E. S. (2013). Molecular evidence for an active endogenous microbiome beneath glacial ice. *The ISME Journal*, *7*(7), 1402–12. https://doi.org/10.1038/ismej.2013.31

Jacques, C., Gkritzalis, T., Tison, J.-L., Hartley, T., van der Veen, C., Röckmann, T., et al. (2020). Carbon and Hydrogen Isotope Signatures of Dissolved Methane in the Scheldt Estuary. *Estuaries and Coasts*. https://doi.org/10.1007/s12237-020-00768-3

Kellerman, A. M., Hawkings, J. R., Wadham, J. L., Kohler, T. J., Stibal, M., Grater, E., et al. (2020). Glacier outflow dissolved organic matter as a window into seasonally changing carbon sources: Leverett Glacier, Greenland. *Journal of Geophysical Research: Biogeosciences*, 1–16. https://doi.org/10.1029/2019jg005161

Kohler, T. J., Žárský, J. D., Yde, J. C., Lamarche-Gagnon, G., Hawkings, J. R., Tedstone, A. J., et al. (2017). Carbon dating reveals a seasonal progression in the source of particulate organic carbon exported from the Greenland Ice Sheet. *Geophysical Research Letters*, *44*(12), 6209–6217. https://doi.org/10.1002/2017GL073219

Lamarche-Gagnon, G., Wadham, J. L., Sherwood Lollar, B., Arndt, S., Fietzek, P., Beaton, A. D., et al. (2019). Greenland melt drives continuous export of methane from the ice-sheet bed. *Nature*, *565*(7737), 73–77. https://doi.org/10.1038/s41586-018-0800-0

Magen, C., Lapham, L. L., Pohlman, J. W., Marshall, K., Bosman, S., Casso, M., & Chanton, J. P. (2014). A simple headspace equilibration method for measuring dissolved methane. *Limnology and Oceanography: Methods*, *12*(9), 637–650. https://doi.org/10.4319/lom.2014.12.637

Michaud, A. B., Dore, J. E., Achberger, A. M., Christner, B. C., Mitchell, A. C., Skidmore, M. L., et al. (2017). Microbial oxidation as a methane sink beneath the West Antarctic Ice Sheet. *Nature Geoscience*, *10*(8), 582–586. https://doi.org/10.1038/ngeo2992

Naus, S., Röckmann, T., & Popa, M. E. (2018). The isotopic composition of CO in vehicle exhaust. *Atmospheric Environment*, *177*, 132–142. https://doi.org/10.1016/j.atmosenv.2018.01.015

Pain, A. J., Martin, J. B., Martin, E. E., & Rahman, S. (2020). Heterogenous CO 2 and CH 4 content of glacial meltwater of the Greenland Ice Sheet and implications for subglacial carbon processes. *The Cryosphere*, (July), 1–33. https://doi.org/10.5194/tc-2020-155

Pataki, D. E., Ehleringer, J. R., Flanagan, L. B., Yakir, D., Bowling, D. R., Still, C. J., et al.

(2003). The application and interpretation of Keeling plots in terrestrial carbon cycle research. *Global Biogeochemical Cycles*, *17*(1). https://doi.org/10.1029/2001GB001850

Pathirana, S. L., van der Veen, C., Popa, M. E., & Röckmann, T. (2015). An analytical system for stable isotope analysis on carbon monoxide using continuous-flow isotope-ratio mass spectrometry. *Atmospheric Measurement Techniques*, *8*(12), 5315–5324. https://doi.org/10.5194/amt-8-5315-2015

Röckmann, T., Eyer, S., van der Veen, C., Popa, M. E., Tuzson, B., Monteil, G., et al. (2016). In situ observations of the isotopic composition of methane at the Cabauw tall tower site. *Atmospheric Chemistry and Physics*, *16*(16), 10469–10487. https://doi.org/10.5194/acp-16-10469-2016

Sapart, C. J., van der Veen, C., Vigano, I., Brass, M., van de Wal, R. S. W., Bock, M., et al. (2011). Simultaneous stable isotope analysis of methane and nitrous oxide on ice core samples. *Atmospheric Measurement Techniques*, *4*(12), 2607–2618. https://doi.org/10.5194/amt-4-2607-2011

Souchez, R., Lemmens, M., & Chappellaz, J. (1995). Flow-induced mixing in the GRIP basal ice deduced from the CO2 and CH4 records. *Geophysical Research Letters*, *22*(1), 41–44. https://doi.org/10.1029/94GL02863

Stibal, M., Wadham, J. L., Lis, G. P., Telling, J., Pancost, R. D., Dubnick, A., et al. (2012). Methanogenic potential of Arctic and Antarctic subglacial environments with contrasting organic carbon sources. *Global Change Biology*, *18*(11), 3332–3345. https://doi.org/10.1111/j.1365-2486.2012.02763.x

Wadham, J. L., Tranter, M., Tulaczyk, S., & Sharp, M. (2008). Subglacial methanogenesis: A potential climatic amplifier? *Global Biogeochemical Cycles*, *22*(2), n/a-n/a. https://doi.org/10.1029/2007GB002951

Wadham, J. L., Arndt, S., Tulaczyk, S., Stibal, M., Tranter, M., Telling, J., et al. (2012). Potential methane reservoirs beneath Antarctica. *Nature*, *488*(7413), 633–637. https://doi.org/10.1038/nature11374

Wadham, J. L., Hawkings, J. R., Tarasov, L., Gregoire, L. J., Spencer, R. G. M., Gutjahr, M., et al. (2019). Ice sheets matter for the global carbon cycle. *Nature Communications*, *10*(1), 3567. https://doi.org/10.1038/s41467-019-11394-4

Whiticar, M. J. (1999). Carbon and hydrogen isotope systematics of bacterial formation and oxidation of methane. *Chem. Geol.*, *161*(1–3), 291–314. https://doi.org/10.1016/S0009-2541(99)00092-3

Yamamoto, S., Alcauskas, J. B., & Crozier, T. E. (1976). Solubility of methane in distilled water and seawater. *Journal of Chemical & Engineering Data*, *21*(1), 78–80. https://doi.org/10.1021/je60068a029

Captions

Figure 5 Top panel: Map of West Greenland and Isunnguata glacier with study site indicated at red squares (top left inset) and an overview of the study site at the ice front in June 2018. Letters

(a, b, c) indicate location of measurement of mole fractions of CH_4 and CO_2 in subglacial air and sampling of melt water at three different stages during the melt season. a) May 2019 represents the early stage meltwater discharge where the meltwater openings are small and mostly filled with water. b) June 2018 represents a progressive stage of opening where multiple cracks and caves are air filled after the meltwater has carved out channels in the ice. c) August 2018 represents the mature stage of evolution of the meltwater channel, where the volume of the outlet is at its maximum and most of it is air filled due to decreasing meltwater volumes.

Figure 6 Upper panels (a-c): Time series of gaseous mole fractions of CH_4 (green) and CO_2 (grey) in a) June 2018, b) August 2018 and c) May 2019. Black dashed line indicates the atmospheric mole fractions of CH_4 (2 ppm) and CO_2 (400 ppm) measured on site. Lower panels (d-f): Dissolved CH_4 concentrations at three distances (● PW1: 0 m from outlet; ◆ PW2: 200 m from the outlet; ▲ PW3: 2000 meter from the outlet) for d) June 2018, e) August 2018 and f) May 2019. Black dashed line indicates the estimated dissolved concentration of CH_4 at atmospheric equilibrium (0.02 µmol L^{-1}).

Figure 7 Dual isotope plot of Keeling plot estimates of the isotope source signatures ($\delta^{13}C$-CH_4 and $\delta^{2}H$-CH_4) for gCH_4 (transparent symbols and white marker line) in June 2018 (circles) and August 2018 (diamonds). Standard errors of the estimate of isotopic signature (gCH_4) are shown as error bars. Isotopic composition ($\delta^{13}C$-CH_4 and $\delta^{2}H$-CH_4) of dCH_4 are shown in white symbols with black edge for June 2018 (circles) and August 2018 (diamonds) campaigns. Grey shaded areas modified after Whiticar (1999). For comparison to the isotopic composition of dCH_4 and signature of gCH_4 the $\delta^{13}C$ and $\delta^{2}H$ values of atmospheric CH_4 are shown with X's.

Figure 8 a) Temporal variation of isotopic ($\delta^{13}C$) source signatures for gaseous CO_2 (◆) and CH_4 (●) and the isotopic composition of dissolved subglacial CH_4 (○). Subglacial gaseous CO_2 mole fractions (ppm) are superimposed as grey line. Vertical error bars for gCO_2 and gCH_4 indicate the standard error of the Keeling plot intercept; in most cases error bars were smaller than the symbols. indicate the $\delta^{13}C$ values of atmospheric CO_2 (orange) and CH_4 (green), respectively and b) Dual isotope plots showing the resulting Keeling plot isotope signature of gCO_2 ($\delta^{13}C$-CO_2) plotted against the isotopic signature of gCH_4 (orange diamonds). Standard errors of the Keeling plot intercept are shown as vertical and horizontal error bars. In most cases error bars were smaller than the symbols.

Table 3 Average, minimum and maximum gaseous subglacial CH_4 and CO_2 mole fractions in May 2019, June 2018 and August 2018 campaigns. *The enrichment factor (xAtmosphere) relative to the atmosphere for CH_4 and CO_2 is based on in situ measurements of the atmospheric molefractions of CH_4 = 2 ppm and CO_2= 400 ppm.

Table 4 Emission range estimates of CH_4 and CO_2 for the non-water filled cross section of the subglacial river outlet for the May 2019, June 2018 and August 2018 campaigns.